IEEE Photonics Journal
An IEEE Photonics Society Publication
Open Access

IEEE Xplore® Digital Library
http://ieeexplore.ieee.org/Xplore

Fourier Single-pixel Imaging Based on Lateral Inhibition for Low-contrast Scenes

Kaiyu Zhang,[1] Jie Cao,[1,3,*] Fanghua Zhang,[1] Yahui Jiang,[1] Yang Cheng,[1] Dong Wang,[4] Qun Hao,[1,2]

[1]School of Optics and Photonics, Beijing Institute of Technology, Key Laboratory of Biomimetic Robots and Systems, Ministry of Education, Beijing, 100081, China

[2]Graduate School at Shenzhen, Tsinghua University, Shenzhen, 518055, China

[3]NUS Suzhou Research Institute, Suzhou, Industrial Park, Suzhou, 215123, China

[4]Tianjin Institute of Aerospace Mechanical and Electrical Equipment, Tianjin Key Laboratory of Aerospace Intelligent Equipment Technology, Tianjin, 300458, China

Abstract: A Fourier single-pixel imaging technique based on lateral inhibition is proposed to improve the reconstruction contrast and quality for low-contrast scenes. The mathematical models are developed, and corresponding simulations and experiments are conducted to verify and evaluate the features. Results show that this strategy strengthens the image contrast and structural similarity index mainly under low sampling ratios compared with the traditional Fourier single-pixel imaging. It offers an optional solution for various Fourier single-pixel imaging applications at low sampling ratios for low-contrast scenes.

Index Terms: Imaging systems, Computational imaging, Image reconstruction techniques

1. Introduction

Single-pixel imaging (SPI) reconstructs target information by correlating pre-defined patterns projected onto the scene with back-scattered intensity captured by a photodiode. Compared with traditional array imaging technologies such as CCD or CMOS, the SPI may offer better detection efficiency, lower noise and higher time resolution [1]. Considering these benefits, SPI has been applied to many applications such as 2D [2] and 3D imaging [3, 4], multispectral [5] or hyperspectral imaging [6], terahertz imaging [7, 8], remote sensing [9, 10], microscopic imaging [11, 12], and scatter imaging [13, 14].

Improving imaging quality and speed (frames per second) is a research focus in SPI because SPI suffers from long measurement times and weak reconstruction quality by the optical correlation in the early stage [15-18]. The compressive sensing (CS) techniques and basis scan (BS) strategies were mainly introduced to enhance the performance of SPI. CS has proved to be an excellent theoretical framework for SPI because of the natural image's sparse priors [19, 20]. Especially, the CS-based total variation regularization method (TV) has been widely applied to various applications [21, 22]. Although CS recovers higher quality image with lower sampling ratio compared to the optical correlation method, it cannot be applied for real-time high-resolution applications because of high computational cost associated with $\ell 1$-minimization. As an alternative, BS strategies reconstruct the scene by simply inverse transforming the coefficients acquired from a series of basis patterns projected onto the scene [23-28] (e.g. Hadamard, Fourier, wavelet). One of the problems with BS strategies is the long acquisition time. In order to reconstruct a high-resolution scene image, large number of coefficients (measurements) are needed to acquire which thereby increases acquisition time. Recently, adaptive schemes for BS strategies have been proposed to improve the reconstruction efficiency by decreasing the number of the coefficients acquired. Additionally, content-adaptive methods [29, 30], digital microscanning [31], bio-inspired imaging [32-34], increasing the pattern illumination rate [35], and deep learning [36, 37] methods for SPI have also emerged.

From the practical point of view, the reconstruction image quality in SPI is also influenced by the scene's characteristics. Although the difference method [38] and BS strategies decrease the effect of environmental noise to some extent, these techniques do not take into account the features of the target scene, and more specifically for low-contrast scenes. To improve the image quality in low-contrast scenes, lateral inhibition inspired by the biological phenomenon [39] has been applied. Since the visual lateral inhibition was observed in the limulus vision and vision systems of other animals, many mathematical models [40-43] describing this phenomenon are put forward to reduce illumination disturbances and enhance image quality. Lateral inhibition has shown to increase the contrast and sharpness in visual response [44]. However, the lateral inhibition is very sensitive to noises [45]. It will simultaneously amplify noises while accentuating the intensity gradients of image-edges and contours. Hence, it means that if the lateral inhibition model is directly used for the enhancement of low-contrast image reconstructed by SPI, the noises and contours of the reconstruction results will be enhanced.

Owing that SPI can be seen as a weighted sum of 2D pre-defined sampling illumination patterns. It provides a possibility that if the scene based lateral inhibition model is combined with the projected pre-defined patterns, it will only emphasize the sampling of image-edges and enhance contrast. The key to realize this strategy is how to get the scene image as the input

Digital Object Identifier 10.1109/JPHOT.2019.2936862

of the lateral inhibition model. Fortunately, the reconstructed results by the sampled coefficients of Fourier single-pixel imaging (FSI) can provide the scene images as input for the lateral inhibition model with imaging. Combining the reasons above, to improve the image quality of FSI for low-contrast scenes, we propose a Fourier single-pixel imaging technique based on lateral inhibition (LI-FSI), and develop its models to explain its working principle. Several simulations and experiments are conducted to evaluate the features and performance of our proposed method for low-contrast scenes.

2. Mathematical models

The proposed LI-FSI is based on the lateral inhibition model and FSI. The lateral inhibition model indicates that an enhanced gray-scale pixel can be expressed as the sum of its original gray level and a weighted sum of neighboring pixels' gray level by the corresponding lateral inhibition coefficients, according to [43], the general model of lateral inhibition is written as

$$O(x,y) = I(x,y) + \sum_{i=-A}^{A} \sum_{j=-B}^{B} a_{ij} I(x+i, y+j), \quad (1)$$

Where (x,y) represents the 2D Cartesian coordinate, A and B refer to the inhibition scales, $O(x,y)$ is the enhanced pixel gray level, $I(x,y)$ is the original pixel gray level, a_{ij} is the lateral inhibition weight parameter.

The a_{ij} can be selected flexibly by arbitrary distribution, but requires

$$\sum_{i=-A}^{A} \sum_{j=-B}^{B} a_{ij} = 0, \quad (2)$$

which balances the inhibition effects.

On the other hand, FSI is based on the theorem of the Fourier transform. The reconstruction result can be expressed as a weighted sum of $I \times J$ 2D sinusoid structured light patterns by the corresponding Fourier coefficients, which can be denoted as follow [46]:

$$f(x,y) = \frac{1}{IJ} \sum_{u=0,v=0}^{I-1,J-1} F(u,v) \cdot [\cos(\frac{2\pi xu}{I} + \frac{2\pi yv}{J}) + j \cdot \sin(\frac{2\pi xu}{I} + \frac{2\pi yv}{J})], \quad (3)$$

where (u,v) represents the spatial frequency, and $F(u,v)$ is the Fourier coefficient. Thus, the result can be reconstructed by combining the Fourier illumination patterns and the Fourier coefficients calculated by the corresponding light intensities acquired by a single-pixel detector.

Combining with the lateral inhibition and FSI above, we deduce the LI-FSI models as follows. The LI-FSI can be viewed as a weighted sum of $M \times N$ 2D Fourier illumination patterns based on lateral inhibition by the corresponding coefficients. Therefore, we obtain

$$R(x,y) = \frac{1}{MN} \sum_{u=0,v=0}^{M-1,N-1} F_L(u,v) \cdot I_L(x,y;u,v), \quad (4)$$

where $R(x,y)$ is the reconstructed result by LI-FSI, (u,v) represents the spatial frequency, $I_L(x,y;u,v)$ is the Fourier illumination pattern based on lateral inhibition and $F_L(u,v)$ is the corresponding coefficient. Similar to FSI, the reconstruction of LI-FSI also needs to create the modulated patterns and acquire the corresponding coefficients.

$I_L(x,y;u,v)$ as a modulated pattern in the LI-FSI system can be obtained on basis of the Fourier illumination pattern. A Fourier illumination pattern $I_F(x,y;u,v)$ can be generated by applying an 2D-inverse Fourier transform to a delta function $\delta_F(u,v,\varphi)$ [46]

$$I_F(x,y;u,v) = \frac{1}{2} + \frac{1}{2} real(F^{-1}(\delta_F(u,v,\varphi))), \quad (5)$$

where *real*(.) represents the real part, F^{-1}(.) denotes an inverse Fourier transform, the parameter φ represents the initial phase and

$$\delta_F(u,v,\varphi) = \begin{cases} \exp(j\varphi), & u = u_0, v = v_0 \\ 0, & \text{otherwise} \end{cases}. \quad (6)$$

Then, an $I_L(x,y;u,v)$ can be view that the lateral inhibition coefficient matrix calculated by the reconstruction using the previous spatial frequency sampling acts on the next Fourier illumination pattern. Thus, an $I_L(x,y;u,v)$ can be generated by the corresponding Fourier illumination pattern dot-multiplying the lateral inhibition coefficient matrix, which can be expressed as

$$I_L(x,y;u,v) = \begin{cases} I_F(x,y;u,v), & u = 0, v = 0 \\ I_F(x,y;u,v) \cdot L(x,y;u-1,v-1), & u = v, u \neq 0, v \neq 0 \\ I_F(x,y;u,v) \cdot L(x,y;u-1,v), & u > v \\ I_F(x,y;u,v) \cdot L(x,y;u,v-1), & u < v \end{cases}, \quad (7)$$

where $L(x,y;u,v)$ is the lateral inhibition coefficient matrix. It is important to mention that the first Fourier illumination pattern based on lateral inhibition is generated using the traditional FSI pattern (Eq. 7 for u=*0*, v=0). Next, the scene information is first reconstructed by the initial pattern and processed using lateral inhibition to generate lateral inhibition coefficient matrixes and subsequent patterns. $L(x,y;u,v)$ describes the relationship between the enhanced result based on lateral

inhibition and the direct reconstruction by the previous spatial frequency sampling, therefore

$$\begin{aligned} L(x,y;u,v) &= O_F(x,y;u,v)./\,R_S(x,y;u,v) \\ &= [R_S(x,y;u,v) + \sum_{i=-H}^{H}\sum_{j=-K}^{K} \alpha_{ij} R_S(x+i,y+j;u,v)]./\,R_S(x,y;u,v), \end{aligned} \tag{8}$$

where $O_F(x,y;u,v)$ is the enhanced result when $R_S(x,y;u,v)$ as the direct reconstruction image is substituted into the Eq.(1), H and K refer to the inhibition scales. $R_S(x,y;u,v)$ is a single reconstructed result computing by the single Fourier illumination pattern based on lateral inhibition and corresponding coefficient, which can be denoted as

$$R_S(x,y;u,v) = F_L(u,v)\cdot I_L(u,v;x,y), \tag{9}$$

Combining the Eqs. (5)-(9) above, the Fourier illumination pattern based on lateral inhibition $I_L(x,y;u,v)$ can be acquired. For example, Fig. 1 shows a schematic demonstration of a 3 × 3 pixels part of a grayscale Fourier illumination pattern based on lateral inhibition produced by a Fourier illumination pattern and a lateral inhibition coefficient matrix.

255	208	103	·	0.8	0.9	1	=	204	187	103
226	128	28		0.9	1.2	1.1		203	153	31
152	46	0		0.8	1.1	0.9		121	51	0
$I_F(x,y)$				$L(x,y;u\text{-}1,v\text{-}1)$ when $u=v, u\neq 0, v\neq 0$				$I_L(x,y;u,v)$		

Fig. 1 A Fourier illumination pattern based on lateral inhibition produced by a Fourier illumination pattern and a lateral inhibition coefficient matrix.

And then the coefficient $F_L(u,v)$ can be computed similar to FSI as follows.

Assuming the intensity distribution of the light source in LI-FSI system is a Gaussian function, its practical model can be expressed as [47]

$$P(x,y) = P_0 \cdot \exp(-\frac{2\cdot((x-x_c)^2+(y-y_c)^2)}{W_0^{\,2}}), \tag{10}$$

where P_0 denotes the power, (x_c,y_c) represents central Cartesian coordinate and W_0 is the waist radius of the light source. Combining Eqs. (10) & (7), the intensity distribution $P_n(x,y)$ of the pattern that illuminates the target scene can be defined as

$$\begin{cases} P_{\mathrm{n}}(x,y) = \dfrac{1}{2}\cdot\dfrac{W_0^{\,2}}{W_L^{\,2}}\cdot P_0\cdot\exp(-\dfrac{2\cdot((x-x_c)^2+(y-y_c)^2)}{W_L^{\,2}})\cdot I_L(u,v;x,y) \\ W_L = W_0\sqrt{1+\left(\dfrac{\lambda L}{\pi W_0}\right)^2} \end{cases}, \tag{11}$$

where L is the distance between the LI-FSI system and target scene, W_L is the beam waist radius through L. Assuming that $T(x,y)$ is the target reflectivity distribution, the corresponding total light intensity $D_\varphi(u,v)$ acquired by the single-pixel detector is expressed as

$$D_\varphi(u,v) = \sum_{x,y} P_n(x,y)\cdot T(x,y). \tag{12}$$

Accordingly, $F(u,v)$ is required by the different phase-shifting patterns with 4 or 3 measurements:

$$F_L(u,v) = \begin{cases} (D_\pi(u,v) - D_0(u,v)) + \mathrm{j}(D_{3\pi/2}(u,v) - D_{\pi/2}(u,v)), & 4\text{-}step\ FSI \\ (2D_0(u,v) - D_{2\pi/3}(u,v) - D_{4\pi/3}(u,v)) + \sqrt{3}\,\mathrm{j}\cdot(D_{2\pi/3}(u,v) - D_{4\pi/3}(u,v)), & 3\text{-}step\ FSI \end{cases}. \tag{13}$$

Here, $D_0(u,v)$, $D_{\pi/2}(u,v)$, $D_\pi(u,v)$, $D_{3\pi/2}(u,v)$ are the measurements corresponding to the 4-step FSI, and $D_0(u,v)$, $D_{2\pi/3}(u,v)$, $D_{4\pi/3}(u,v)$ are the measurements corresponding to the 3-step FSI, respectively.

3. Experiments

3.1. Computational simulations

First, the Cameraman image is used to verify the proposed models and compare the performance between LI-FSI and FSI through computer simulations. The lateral inhibition weight parameter a_{ij} is generated by the double Gaussian distribution

$$\begin{cases} a_{ij} = \dfrac{1}{\beta}\left\{\dfrac{1}{\beta_1}\cdot\dfrac{1}{\sqrt{2\pi\sigma_1}}\exp\left[\dfrac{(d_{ij}-u_1)^2}{2\sigma_1^{\,2}}\right] - \dfrac{1}{\beta_2}\cdot\dfrac{1}{\sqrt{2\pi\sigma_2}}\exp\left[\dfrac{(d_{ij}-u_2)^2}{2\sigma_2^{\,2}}\right]\right\} \\ d_{ij} = \sqrt{(i-x_r)^2+(j-y_r)^2} \end{cases}, \tag{14}$$

where β, β_1 and β_2 are intensity factors, σ_1 and σ_2 are the standard deviations, u_1 and u_2 are the means and d_{ij} is the Euclidean distance between the 2D Cartesian coordinate (i, j) and the lateral inhibition center (x_r, y_r). For comparison, we manually set β=1, β_1 =2 and β_2=2, u_1= u_2=0, and σ_1 =1 and σ_2 =1.6. The simulation results under 6 different sampling ratios are shown in Fig. 2. The visual subjective perception of the reconstruction images of LI-FSI is better than that of FSI at low sampling ratios and worse at high sampling ratios.

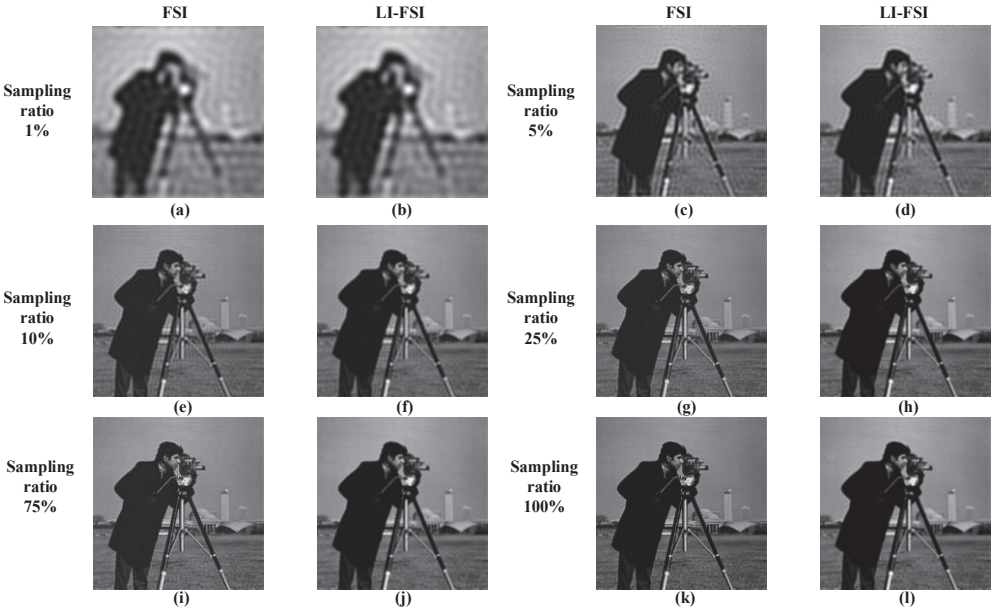

Fig. 2 The reconstructed images by FSI and LI-FSI for cameraman with the sampling ratio ranging from 1% to 100%. The resolution of the reconstructed images is 256 × 256 pixels.

Next, we first use four standard grayscale images (Cameraman, Boat, Fruits and Pens) with different contrast instead of low-contrast scenes as the target scenes to evaluate our proposed method by varying the sampling ratio. For quantitative comparison, we use the contrast and structural similarity index (SSIM) metrics, calculated by:

$$c(r,t)=\frac{2\sigma_r\sigma_t+c_2}{\sigma_r^2+\sigma_y^2+c_2}, \qquad (15)$$

and

$$SSIM(r,t)=\frac{(2\mu_r\mu_t+c_1)(2\sigma_{rt}+c_2)}{(\mu_r{}^2+\mu_t{}^2+c_1)(\sigma_r^2+\sigma_t^2+c_2)}. \quad (16)$$

Here, r and t are the reconstruction result and truth, μ_r and μ_t are their means, σ_r^2 and σ_t^2 are the corresponding variances, σ_{rt} is the covariance of r and t, $c_1=(k_1L)^2$ and $c_2=(k_2L)^2$ are two constants, additionally, L=255, k_1=0.01 and k_2=0.03. The larger the contrast and SSIM values are, the better the reconstruction contrast enhancement and quality are. The contrast and SSIM under 6 different sampling ratios are shown in Table. 1 and Table. 2.

For quantitative comparison, in Table 1 & 2, we highlight the higher contrast and SSIM values produced by the two methods under same sampling ratio. Table. 1 indicates that the reconstruction image contrast values differ among the four scenes and different sampling ratios. The reconstruction image contrast value of LI-FSI is higher than that of FSI under the same sampling ratio. Table. 2 demonstrates that the SSIM values of LI-FSI under low sampling ratios are better than those of FSI. Moreover, the trends of FSI and LI-FSI for the SSIM values of the four targets are nearly consistent respectively. The SSIM values of FSI increase with an increase in sampling ratio. Conversely, the SSIM values of LI-FSI first increases and later decrease. The qualitative and quantitative comparisons show the contrast and SSIM enhancement by LI-FSI at different sampling ratios for different scenes, which benefits the subsequent experiments for low-contrast scenes.

Table. 1 The reconstruction image contrast of FSI and LI-FSI under different scenes and sampling ratios

Scene / Sampling ratio	Cameraman		Boat		Fruits		Pens	
	FSI	LI-FSI	FSI	LI-FSI	FSI	LI-FSI	FSI	LI-FSI
1%	0.209	**0.213**	0.187	**0.189**	0.229	**0.231**	0.198	**0.200**
5%	0.189	**0.201**	0.194	**0.203**	0.224	**0.232**	0.199	**0.211**
10%	0.165	**0.189**	0.194	**0.216**	0.212	**0.234**	0.185	**0.213**
25%	0.168	**0.213**	0.193	**0.231**	0.217	**0.251**	0.208	**0.251**
50%	0.174	**0.205**	0.201	**0.226**	0.210	**0.246**	0.210	**0.243**
75%	0.184	**0.212**	0.212	**0.226**	0.224	**0.249**	0.226	**0.239**
100%	0.185	**0.216**	0.213	**0.228**	0.218	**0.250**	0.224	**0.240**

Table. 2 The reconstruction image SSIM values of FSI and LI-FSI under different scenes and sampling ratios

Scene / Sampling ratio	Cameraman		Boat		Fruits		Pens	
	FSI	LI-FSI	FSI	LI-FSI	FSI	LI-FSI	FSI	LI-FSI
1%	0.498	**0.499**	0.487	**0.489**	0.435	**0.437**	0.473	**0.476**
5%	0.638	**0.656**	0.637	**0.652**	0.611	**0.628**	0.649	**0.677**
10%	0.705	**0.746**	0.735	**0.757**	0.704	**0.755**	0.686	**0.749**
25%	0.802	**0.886**	**0.856**	0.845	0.847	**0.868**	0.821	**0.900**
50%	0.831	**0.839**	**0.885**	0.820	**0.909**	0.857	0.877	**0.888**
75%	**0.879**	0.858	**0.886**	0.789	**0.941**	0.847	**0.901**	0.882
100%	**0.896**	0.858	**0.870**	0.783	**0.942**	0.843	**0.896**	0.878

3.2. Laboratory experiments

The experimental setup is shown in Fig. 3. The setup consists of a DMD-based LED-illumination system, a single-pixel detection system and a target scene. The illumination system is composed of a Texas Instruments DLP LightCrafter 6500 Evaluation Module, a project lens system and a white LED source. The DLP Evaluation Module is comprising of a 0.65-inch 1080p (1920×1080) digital micromirror device (DMD) and a DMD digital controller. The detection system comprises of a Thorlabs PDA36A Si Detector (active area of 13mm^2), a convergent lens system, and a computer equipped with a GaGe Cobra CSE21G8 (1.0 GS/s, 8-bits) digitizer board. The projected FSI and LI-FSI illumination patterns (256 × 256-pixel) are generated by MATLAB program.

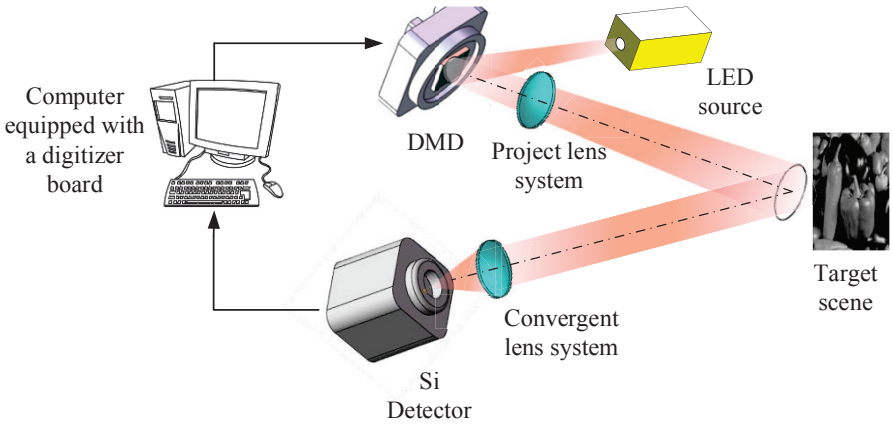

Fig. 3 Experimental setup.

We perform two sets of experiments to validate our proposed strategy. The first is a qualitative imaging experiment to

verify our models. The target scene is a peppers grayscale image printed on a A4-sized white paper. Similar to the simulations, the sampling ratio of the experiment is varied and corresponding reconstruction results (of FSI and LI-FSI) are shown in Fig. 4. As shown in the Fig. 4, the experimental results are consistent with simulation results. From experimental results, it can clearly be seen (Fig. 4 o & p) that the SSIM values of LI-FSI beyond those of FSI under the same low sampling ratios. Although the SSIM values for both methods (FSI and LI-FSI) are almost similar under the same high sampling ratios, our method outperforms FSI in terms of high contrast at different sampling ratios. It proves that the proposed technique can be used to improve the reconstruction contrast and SSIM under low sampling ratios in physical experiments. The images of LI-FSI and FSI are reconstructed using Eq. (3) & (4) respectively. No postprocessing is applied to the reconstructed images.

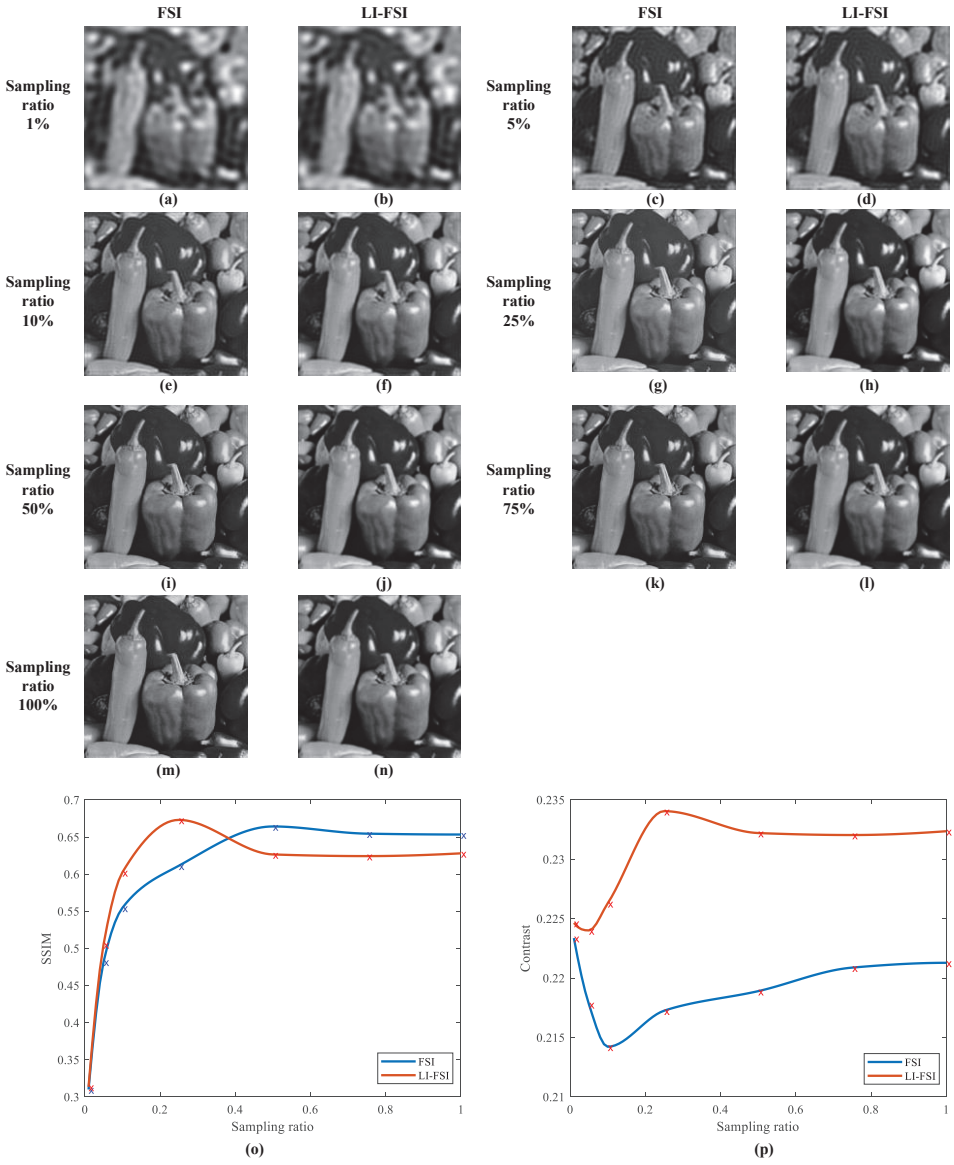

Fig. 4 The comparisons of reconstructed images by FSI and LI-FSI for peppers with the sampling ratio ranging from 1% to 100%. The resolution of the reconstructed images is 256 × 256 pixels. (a)-(n) are the corresponding reconstruction results. (o) and (p) are the curves of the SSIM and the contrast of FSI and LI-FSI with the sampling ratio changing. The mark X denotes the real sampling points.

The second experiment is a quantitative comparison to evaluate the reconstruction performance for low-contrast scenes. For convenient observation, the target scene we chosen consists of four USAF-1951 resolution test patterns with different contrast. These test patterns are in four individual different contrasts: 5%; 33.77%; 70.0% and 91.04%. The other experimental parameters are set as the same as the first. The corresponding results are shown in Fig. 5. The SSIM values of FSI and LI-FSI are nearly the same under low sampling ratios. As the sampling ratio goes up, the SSIM values of LI-FSI are gradually below those of FSI. However, the contrast of LI-FSI still go beyond that of FSI under different sampling ratios.

These two types of experiments demonstrate that LI-FSI improves the reconstruction contrast for low-contrast scenes and outperforms FSI under low sampling ratios. Additionally, Combing the SSIM values of the simulations and experiments, the proposed LI-FSI lags behind FSI under high sampling ratios. This is because that Fourier illumination patterns based on lateral inhibition adopted by LI-FSI emphasize the sampling of image-edges and down sample the neighbor pixels around image-edges, which will lead the sampling loss of the details except image-edges to some extent. Moreover, the lateral

inhibition weight parameter of our simulations and experiments is generated by the double Gaussian distribution, which also smoothes sampling patterns and the reconstruction results causing the details are blurred. Therefore, as the sampling ratio goes up, the feature based on lateral inhibition will limit the increment of the reconstruction image quality causing lagging behind that of FSI.

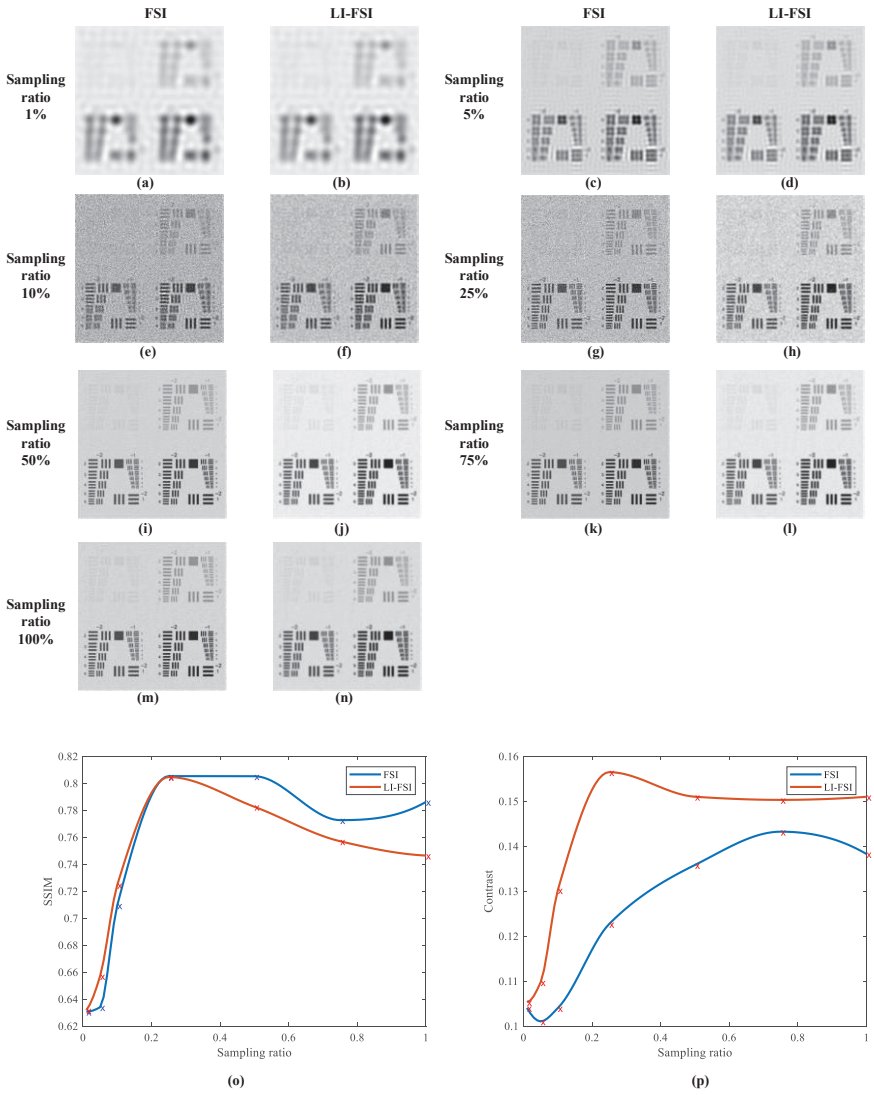

Fig. 5 The comparisons of reconstructed images by FSI and LI-FSI for USAF-1951 resolution test patterns with the sampling ratio ranging from 1% to 100%. The resolution of the reconstructed images is 256 × 256 pixels. (a)-(n) are the corresponding reconstruction results. (o) and (p) are the curves of the SSIM and the contrast of FSI and LI-FSI with the sampling ratio changing. The mark X denotes the real sampling points.

4. Conclusion

We propose an LI-FSI model to improve the reconstruction contrast and performance for low-contrast scenes. In our proposed method, the traditional Fourier illumination patterns are replaced by the Fourier illumination patterns based on lateral inhibition for target scanning, which takes the advantage of image contrast and quality enhancement using lateral inhibition. Through extensive simulations and experiments we find that LI-FSI enhances the reconstruction contrast under different sampling ratios. Objectively, our method performs better than FSI under lower sampling ratios. We conclude that overall our algorithm gives higher SSIM/contrast values at the sampling ratio up to 25% compared to FSI. However, as the sampling ratio goes up (25-100%), the reconstruction results of both methods are almost identical, with LI-FSI outperforming FSI for some target scenes (Table. 2 sampling ratio 50%, pens image). With the sampling ratio increasing, the reconstruction quality of LI-FSI is gradually lower than that of FSI. However, LI-FSI still offers an optional imaging solution because FSI with low sampling ratios is widely used in dynamic imaging and other real imaging applications. In general, the proposed LI-FSI model provides an alternative approach to increase the reconstruction contrast for low-contrast scenes especially under low sampling ratios.

Acknowledgements

National Science Foundation (NSF) (61735003 and 61605008); Beijing Natural Science Foundation (4182058); The Shenzhen Science and Technology Innovation Program (JCYJ20170412171011187).
The authors also wish to thank Saad Rizvi and the anonymous reviewers for their valuable suggestions.

References

[1] M.-J. Sun and J.-M. Zhang, "Single-pixel imaging and its application in three-dimensional reconstruction: a brief review," Sensors, vol. 19, no. 3, p. 732, 2019.
[2] S. S. Welsh, M. P. Edgar, R. Bowman, P. Jonathan, B. Sun, and M. J. Padgett, "Fast full-color computational imaging with single-pixel detectors," Optics express, vol. 21, no. 20, pp. 23068-23074, 2013.
[3] B. Sun et al., "3D computational imaging with single-pixel detectors," Science, vol. 340, no. 6134, pp. 844-847, 2013.
[4] Y. Zhang, M. P. Edgar, B. Sun, N. Radwell, G. M. Gibson, and M. J. Padgett, "3D single-pixel video," Journal of Optics, vol. 18, no. 3, p. 035203, 2016.
[5] L. Bian et al., "Multispectral imaging using a single bucket detector," Scientific reports, vol. 6, p. 24752, 2016.
[6] F. Magalhães, F. M. Araújo, M. Correia, M. Abolbashari, and F. Farahi, "High-resolution hyperspectral single-pixel imaging system based on compressive sensing," Optical Engineering, vol. 51, no. 7, p. 071406, 2012.
[7] W. L. Chan, K. Charan, D. Takhar, K. F. Kelly, R. G. Baraniuk, and D. M. Mittleman, "A single-pixel terahertz imaging system based on compressed sensing," Applied Physics Letters, vol. 93, no. 12, p. 121105, 2008.
[8] C. M. Watts et al., "Terahertz compressive imaging with metamaterial spatial light modulators," Nature Photonics, vol. 8, no. 8, p. 605, 2014.
[9] J. Ma, "Single-pixel remote sensing," IEEE Geoscience and Remote Sensing Letters, vol. 6, no. 2, pp. 199-203, 2009.
[10] J. Ma, "A single-pixel imaging system for remote sensing by two-step iterative curvelet thresholding," IEEE Geoscience and Remote Sensing Letters, vol. 6, no. 4, pp. 676-680, 2009.
[11] N. Radwell, K. J. Mitchell, G. M. Gibson, M. P. Edgar, R. Bowman, and M. J. Padgett, "Single-pixel infrared and visible microscope," Optica, vol. 1, no. 5, pp. 285-289, 2014.
[12] A. Rodríguez, P. Clemente, E. Tajahuerce, and J. Lancis, "Dual-mode optical microscope based on single-pixel imaging," Optics and Lasers in Engineering, vol. 82, pp. 87-94, 2016.
[13] E. Tajahuerce et al., "Image transmission through dynamic scattering media by single-pixel photodetection," Optics Express, vol. 22, no. 14, pp. 16945-16955, 2014.
[14] V. Durán et al., "Compressive imaging in scattering media," Optics express, vol. 23, no. 11, pp. 14424-14433, 2015.
[15] T. Pittman, Y. Shih, D. Strekalov, and A. Sergienko, "Optical imaging by means of two-photon quantum entanglement," Physical Review A, vol. 52, no. 5, p. R3429, 1995.
[16] A. Gatti, E. Brambilla, M. Bache, and L. A. Lugiato, "Ghost imaging with thermal light: comparing entanglement and classical correlation," Physical review letters, vol. 93, no. 9, p. 093602, 2004.
[17] R. H. Hadfield, "Single-photon detectors for optical quantum information applications," Nature photonics, vol. 3, no. 12, p. 696, 2009.
[18] B. I. Erkmen and J. H. Shapiro, "Ghost imaging: from quantum to classical to computational," Advances in Optics and Photonics, vol. 2, no. 4, pp. 405-450, 2010.
[19] M. F. Duarte et al., "Single-pixel imaging via compressive sampling," IEEE signal processing magazine, vol. 25, no. 2, pp. 83-91, 2008.
[20] R. M. Willett, R. F. Marcia, and J. M. Nichols, "Compressed sensing for practical optical imaging systems: a tutorial," Optical Engineering, vol. 50, no. 7, p. 072601, 2011.
[21] F. Magalhães, F. M. Araújo, M. V. Correia, M. Abolbashari, and F. Farahi, "Active illumination single-pixel camera based on compressive sensing," Applied optics, vol. 50, no. 4, pp. 405-414, 2011.
[22] R. F. Marcia, R. M. Willett, and Z. T. Harmany, "Compressive optical imaging: architectures and algorithms," Optical and Digital Image Processing: Fundamentals and Applications, pp. 485-505, 2011.
[23] S. S. Welsh, M. P. Edgar, R. Bowman, B. Sun, and M. J. Padgett, "Near video-rate linear Stokes imaging with single-pixel detectors," Journal of Optics, vol. 17, no. 2, p. 025705, 2015.
[24] Z. Zhang, X. Ma, and J. Zhong, "Single-pixel imaging by means of Fourier spectrum acquisition," Nature communications, vol. 6, p. 6225, 2015.
[25] F. Rousset, N. Ducros, A. Farina, G. Valentini, C. D'Andrea, and F. Peyrin, "Adaptive basis scan by wavelet prediction for single-pixel imaging," IEEE Transactions on Computational Imaging, vol. 3, no. 1, pp. 36-46, 2016.
[26] L. Wang and S. Zhao, "Fast reconstructed and high-quality ghost imaging with fast Walsh–Hadamard transform," Photonics Research, vol. 4, no. 6, pp. 240-244, 2016.
[27] M. Alemohammad, J. R. Stroud, B. T. Bosworth, and M. A. Foster, "High-speed all-optical Haar wavelet transform for real-time image compression," Optics express, vol. 25, no. 9, pp. 9802-9811, 2017.
[28] K. M. Czajkowski, A. Pastuszczak, and R. Kotyński, "Single-pixel imaging with Morlet wavelet correlated random patterns," Scientific reports, vol. 8, no. 1, p. 466, 2018.
[29] Z. Li, J. Suo, X. Hu, and Q. Dai, "Content-adaptive ghost imaging of dynamic scenes," Optics express, vol. 24, no. 7, pp. 7328-7336, 2016.
[30] H. Jiang, S. Zhu, H. Zhao, B. Xu, and X. Li, "Adaptive regional single-pixel imaging based on the Fourier slice theorem," Optics express, vol. 25, no. 13, pp. 15118-15130, 2017.
[31] M.-J. Sun, M. P. Edgar, D. B. Phillips, G. M. Gibson, and M. J. Padgett, "Improving the signal-to-noise ratio of single-pixel imaging using digital microscanning," Optics express, vol. 24, no. 10, pp. 10476-10485, 2016.
[32] D. B. Phillips et al., "Adaptive foveated single-pixel imaging with dynamic supersampling," Science advances, vol. 3, no. 4, p. e1601782, 2017.
[33] M.-J. Sun, X.-Y. Zhao, and L.-J. Li, "Imaging using hyperuniform sampling with a single-pixel camera," Optics letters, vol. 43, no. 16, pp. 4049-4052, 2018.
[34] K. Zhang, J. Cao, Q. Hao, F. Zhang, Y. Feng, and Y. Cheng, "Modeling and Simulations of Retina-Like Three-Dimensional Computational Ghost Imaging," IEEE Photonics Journal, vol. 11, no. 1, pp. 1-13, 2019.
[35] Z.-H. Xu, W. Chen, J. Penuelas, M. Padgett, and M.-J. Sun, "1000 fps computational ghost imaging using LED-based structured illumination," Optics express, vol. 26, no. 3, pp. 2427-2434, 2018.
[36] M. Lyu et al., "Deep-learning-based ghost imaging," Scientific reports, vol. 7, no. 1, p. 17865, 2017.
[37] C. F. Higham, R. Murray-Smith, M. J. Padgett, and M. P. Edgar, "Deep learning for real-time single-pixel video," Scientific reports, vol. 8, no. 1, p. 2369, 2018.
[38] F. Ferri, D. Magatti, L. Lugiato, and A. Gatti, "Differential ghost imaging," Physical review letters, vol. 104, no. 25, p. 253603, 2010.
[39] H. K. Hartline and C. H. Graham, "Nerve impulses from single receptors in the eye," Journal of Cellular and Comparative Physiology, vol. 1, no. 2, pp. 277-295, 1932.
[40] H. K. Hartline and F. Ratliff, "Spatial summation of inhibitory influences in the eye of Limulus, and the mutual interaction of receptor units," The Journal of general physiology, vol. 41, no. 5, pp. 1049-1066, 1958.
[41] H. Fu and D. Li, "The Application of Lateral Inhibition Model in Image's Contour Enhancement and Design of Its Electro-Model," Journal of Multimedia, vol. 4, no. 6, 2009.
[42] L. Gan and H. Duan, "Biological image processing via Chaotic Differential Search and lateral inhibition," Optik-International Journal for Light and Electron Optics, vol. 125, no. 9, pp. 2070-2075, 2014.
[43] S. Dai, Q. Liu, P. Li, J. Liu, and H. Xiang, "Study on infrared image detail enhancement algorithm based on adaptive lateral inhibition network," Infrared Physics & Technology, vol. 68, pp. 10-14, 2015.
[44] G. A. Fry, "Mechanisms subserving simultaneous brightness contrast," Optometry and Vision Science, vol. 25, no. 4, pp. 162-178, 1948.
[45] B. Li, Y. Li, H. Cao, and H. Salimi, "Image enhancement via lateral inhibition: An analysis under illumination changes," Optik, vol. 127, no. 12, pp. 5078-5083, 2016.
[46] J. Huang, D. Shi, K. Yuan, S. Hu, and Y. Wang, "Computational-weighted Fourier single-pixel imaging via binary illumination," Optics express, vol. 26,

no. 13, pp. 16547-16559, 2018.
[47]J. Marques et al., "Temporal and spatial measurements of the electron density perturbation produced in the wake of an ultrashort laser pulse," Physical review letters, vol. 76, no. 19, p. 3566, 1996.